Chapter 6

Force Measuring System for High-Precision Surface Characterization under Extreme Conditions

Roman Nevshupa and Marcello Conte

Additional information is available at the end of the chapter

http://dx.doi.org/10.5772/62386

Abstract

Force measuring is used in various surface characterization techniques such as indentation, scratch tests, tribological analysis, determination of gas content, etc. The main problems related with force measurement under extreme conditions have been analysed. A strategy that should be followed to solve these problems has been discussed and several examples of successive solutions that recently were developed by the authors are presented. The need to carry out the characterization under extreme conditions poses serious problems for the designers of the measuring systems that may include the incompatibility of the sensors with the test conditions, undesirable interactions with other components, stability, precision and uncertainty issues, the measurement range, etc. Resolving these problems must be based on a global approach in which the characterization system is considered as a whole, while the designer must analyse and solve the possible conflicts between the subsystems. The way how an appropriate force measuring system can be selected is described. The proposed method is illustrated by an example in which an indirect force measurement using optical fibre displacement sensor was used. Another example describes measuring system developed for vacuum high-temperature nanoindentation. At high temperature, proper heat management based on non-contact heating and laminar flow cooling system is mandatory to avoid experimental data being affected by external noise and thermal drift.

Keywords: Force sensor, Uncertainty, Modelling, Extreme conditions, Vacuum, High-Temperature Nanoindentation

1. Introduction

Like aerospace industry itself, vacuum tribology rapidly developed in the middle of the twentieth century pursuing to cover the needs in this growing sector in reliable durable materials and

lubricants suitable for operating under vacuum and rarefied gas atmosphere [1–3]. By the 1970s, when some of the problems had been resolved and the limitations of other had been defined, further development of vacuum tribological techniques slowed down [4]. The situation changed in 1990s driven by the advancements in various sectors including semiconductor, energy, transport, etc. that issued new challenges for development of materials with controlled micro- and nanostructure for extreme operation conditions. For example, advanced tribological materials for space applications must comply with very strict requirements on strength, toughness, and wear resistance and also have low outgassing, emission of volatiles, high chemical stability, low secondary electron emission, etc. [3,5,6]. Moreover, in semiconductor industry gaseous and particular contamination associated with tribochemical degradation and wearing of materials in tribo-contacts of mechanical components is one of the main problems that interferes development of fully automatic robotized technological lines with enhanced production yield.

Surface mechanical characterization in vacuum such as precise tribometry, indentation, scratching, etc. is now enjoining a renaissance with various new techniques developed in the last three decades [4,7–9]. These new techniques have been evolved towards both enhancement of their features and integration with other techniques. Combination of mechanical , physical and chemical characterization [4] has offered the opportunity to study complex processes of gas-phase lubrication [10], mechanically stimulated gas emission [4,11–13], triboplasma [14–16], triboelectrification [17], triboluminescence [15,16,18], emission of charged particles [19,20], tribochemical reactions [21–25], and so on. On the other hand, nanoindentation has become widespread as a method to study the mechanical response of materials [26], particularly the measurement of hardness [27,28], elastic modulus [27,28], hardening exponents [29], creep parameters [30], and residual stresses [31]. For all of these purposes, however, nanoindentation testing has most commonly been conducted at room temperature. This is in spite of the fact that micro-materials and devices are often employed at elevated temperatures, and deformation physics are usually thermally activated. The use of nanoindentation to study materials and thin films at high temperature is of high interest and undergo through several limitation due to material oxidation, thermal drift, and machine stability [32].

Therefore, development of precise and reliable measuring systems for force and displacement that must be compatible with extreme operating conditions and with other instruments for physico-chemical characterization is crucial for overall performance of the techniques. In this work we summarize some recent advances in development of force measuring systems for high-temperature nanoindentation and ultrahigh vacuum tribometry.

2. Problems and challenges of measuring systems under extreme conditions: resolving the conflicts

2.1. Ultrahigh vacuum tribology

Force transducers suitable for ultrahigh vacuum applications must comply not only with the requirements on rated capacity, non-linearity, combined error, repeatability, reproducibility,

http://dx.doi.org/10.5772/62386

creep, long-term stability, frequency response, fatigue life, etc. but also with a series of specific provisions [33]. Among others these provisions include possibility of outgassing baking, reduced emission rate of volatiles and gas desorption, appropriate thermal management and heat sinks in absence of convection and heat conduction through the air, low emission of electromagnetic interferences that could affect other neighbour analytic tools, low emission of gases and volatiles, and so on. For example, strain gauges, capacitive, and inductive transducers can cause crosstalk in charge detectors, electron multipliers, antennas and other sensitive electromagnetic devices. Force transducers that utilize visible light may alter the measurements of triboluminescence by introducing undesirable background radiation.

In general, selection and development of the transducers for measuring system being used under vacuum must be done using holistic approach in which a satisfactory compromise between the requirements set by various subsystems of the entire test rig upon the environmental and operational conditions, relative position of the components and their compatibility must be found. A design of the tests rig in which such satisfactory compromise is achieved is considered as optimal. Recently it was shown that an experimental system for combined tribological and , physical and chemical characterization normally comprises seven subsystems one of which is the measurement system [4]. Therefore, optimal design must involve matching the measuring systems with other six subsystems including vacuum, mechanical, sample handling, environmental control, loading, and kinematics and physico-chemical characterization (**Figure 1**).

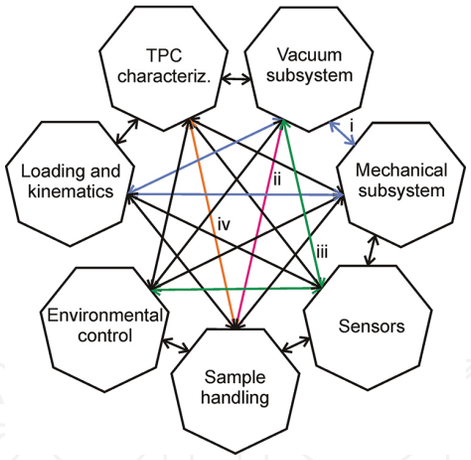

Figure 1. Subsystems of a vacuum test rig for complex tribological and tribo-physico-chemical (TPC) characterization of materials. Some of the critical relationships and constrictions between the subsystems are shown by arrows: i (blue) – limitations between Vacuum, Mechanical, and Loading and Kinematics subsystems; ii (red) – limitations between Vacuum and Sample handling subsystems; iii (green) – limitations between Sensors, Environmental control, and Vacuum subsystems; iv (orange) – limitations between Sample handling and TPC subsystems. (Reprinted from [4] Copyright 2015, with permission from Elsevier.)

2.2. Nanoindentation at high and low temperatures

In normal ambient conditions most of metallic materials, semiconductors, metal hydrides, etc., when heated up, experience oxidation. In many cases an oxide layer at elevated temperature

can be as thick as the penetration depth of a tip. This poses serious problem for material characterization through nanoindentation since the measured hardness value may correspond to the oxide layer rather than to the substrate. To avoid oxidation the measurement should be done in inert environment or in high vacuum. The latter is preferable because of the higher surface cleanliness. Also, in absence of convection in vacuum more precise and efficient heating control can be achieved. Vacuum is also desirable when indentation must be carried out at cryogenic temperatures. In this case, vacuum is needed to avoid condensation and to cut down thermal flow towards cold surfaces through conductivity and convection. Nevertheless, an increase the complexity of the experimental system by adding subsystems, e.g. pumping means, vacuum measurement, etc. can introduce important external noise or limit the system functionality. For example, the materials being tested must be vacuum compatible, i.e. to have sufficiently low pressure of saturated vapours at given temperature in order to reach the required vacuum degree. Another important problem is related with deformations of the system components due to differences in thermal expansion of construction materials. The components of the measurement system may be subjected to important temperature gradients when a pin and material at the indentation zone are heated up or cooled down, while some sensitive elements including electronic circuits situated in proximity to the indentation zone have to be maintained at room temperature. When temperature distribution in the components of the measuring system is non-stationary it can lead to thermal drift. Therefore, the collected data, in general, is a complex function of the mechanical behaviour of material under study, fluctuations and noise induced due to operation of subsystems, and thermal drift. Measurement uncertainties and errors associated with fluctuations, noise and thermal drift can be significantly reduced by correct designing of the measurement system. Analysis of some problems that must be solved to achieve the optimal design and possible solutions are discussed in Section 3.

3. Nanoindentation at high temperature

Development of turbomolecular pumping system with a magnetically suspended rotor (maglev) and oil-less primary pump has offered a cost-effective and clean solution for those applications where vibration is a serious problem. By combining opportune materials with maglev pumping system it is possible to significantly dump vibrations in nanoindentation systems. Nevertheless, it is not enough when vibrations due to thermal expansion happen. An interesting solution was presented in [34,35]. It is based on an active top referencing configuration which eliminates almost entirely the problem of noise and, furthermore, reduces to negligible values the instrument frame compliance. Such substantial improvement has been achieved by the use of a unique principle of load and displacement measurements. So far all existing nanoindentation systems have been based on only one actuator and one sensor. The ultra nanoindentation method uses two separated actuators and three separated sensors, which provide real measurements of depth and load, as well as a feedback loop that allows continuous and accurate control of the applied load (**Figure 2**). In particular, each axis has its own actuator, displacement and load sensors. For both axes, the displacement is applied via piezo actuators A1 and A2. The load on the indenter and the reference is obtained from the

http://dx.doi.org/10.5772/62386

displacement of the springs K1 and K2, measured with capacitive sensors C1 and C2. The displacement of the indenter is measured relative to the reference through the differential capacitive sensor C3.

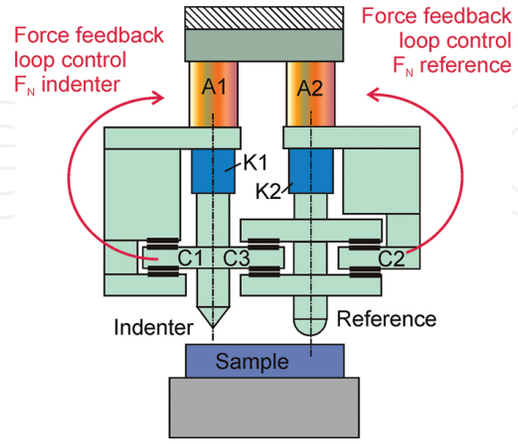

Figure 2. Schematic design of Ultra Nanoindentation head. F_N – normal load; A1 – Indenter's piezo actuator; A2 – Reference's piezo actuator; K1 – Indenter's load cell spring; K2 – Reference's load cell spring; C1 – Indenter's load cell capacitive sensor; C2 – Reference's load cell capacitive sensor; C3 – Penetration depth differential capacitive sensor.

Continuous control of normal force on both the indenter and the reference is ensured by precise feedback loops. The crucial components used in the measurement head are made of Zerodur®, a material with extremely low coefficient of thermal expansion (0.01×10^{-6} K^{-1} over the range 0 °C – 100 °C).

Considering it as a starting point, addressing the thermal drift problem is the next step before performing high precision nanoindentation tests. The need to reduce the thermal flow at the contact point can be achieved in two ways called passive heating and active heating, respectively. The former is based on holding the indenter in contact with the sample surface for a time long enough to equilibrate the temperature of the involved bodies. The latter consist of heating up the involved bodies independently. This was demonstrated to be the most appropriate way, especially for temperature higher than 400 °C, that is, when incandescence becomes important [8]. In the same work, the effect of thermal drift on the elastic modulus and hardness measurements on standard reference materials has been analysed.

Heating the sample to be characterized is not a difficult task as any contact/non-contact heating system can be used. However, heating the indentation tip is not easy as any contact acts as a spring and its compliance can be read out by the force and displacement sensors. A non-contact heating system is then preferred.

In [9] a novel patent pending non-contact heating system based on IR radiation was presented (**Figure 3**). The main advantage of IR heaters is their almost zero thermal inertia. Such heating system located in high vacuum environment uses the active top referencing system previously illustrated for high temperature nanoindentation. The reference and indenter shafts are irradiated independently by infrared emitters and their temperatures are read out by means of thermocouples embedded in the tips. When the sample approaches the measurement

device, an IR bath is established allowing a fast and precise regulation of the sample surface temperature. Opportune reflective coatings and water cooling management in the measurement area allow reaching accuracy of temperature about 0.1 °C, that is the accuracy of the thermocouples at temperatures as high as 800 °C.

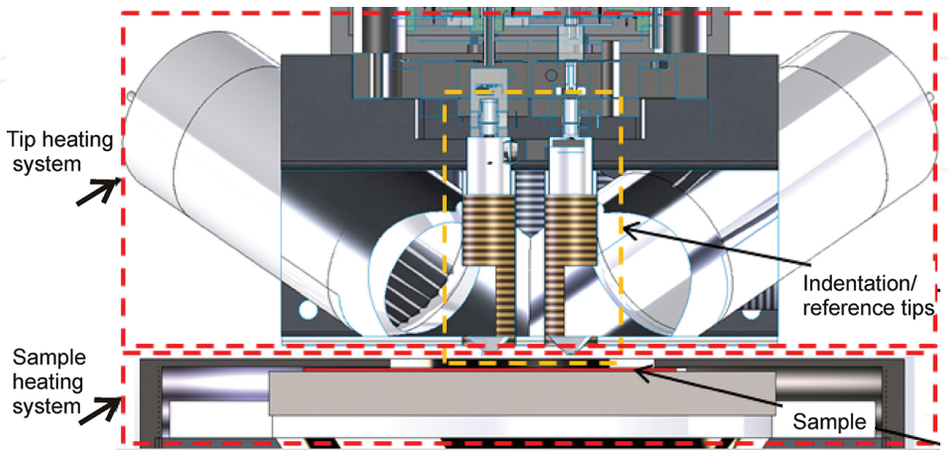

Figure 3. Schematic drawing of the sample and tip heating systems.

Thermal drift rate was measured on oxygen free high conductivity copper (OFHC Cu) by loading up to 100 mN in at least 30 s, holding the maximum load for few seconds and unloading to 5 mN, that is less than 10% of the maximum load to avoid material creep (**Figure 4**). The indenter was hold in contact for 1 minute and the deviation of the penetration depth was measured along this period. A thermal drift less than 1 nm/min was recorded for all the measurements up to 600 °C (**Figure 5**).

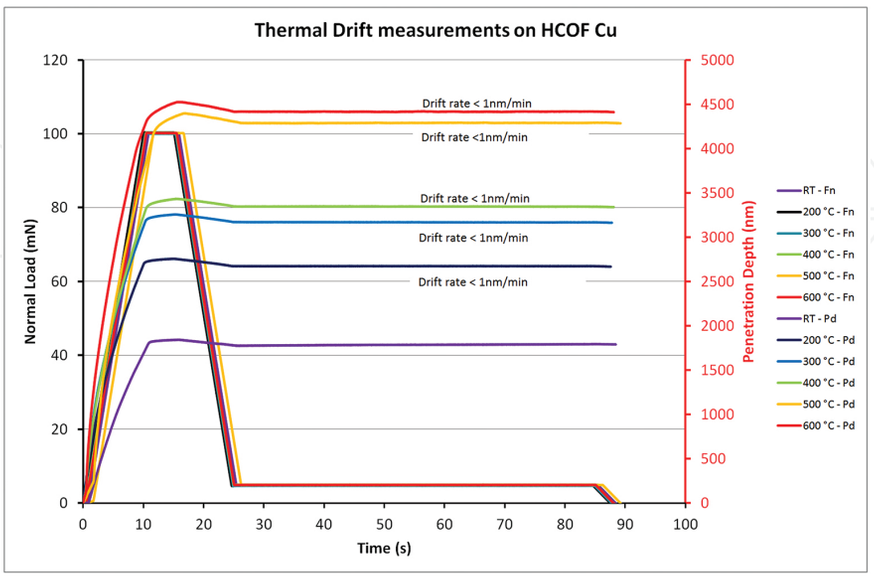

Figure 4. Thermal drift of the measuring system registered under various loads and temperatures.

http://dx.doi.org/10.5772/62386

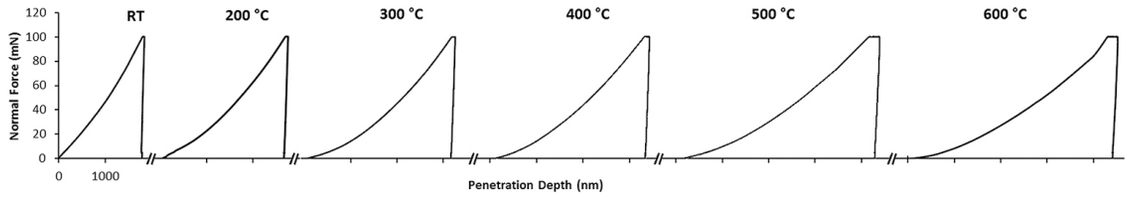

Figure 5. Indentation tests on oxygen free high conductivity copper at various temperatures.

The extrapolation of Elastic Modulus and Hardness from the uncorrected data is then an easy task.

4. Force transducers for tribological and physicochemical characterization in ultrahigh vacuum

4.1. Force measurement in ultrahigh vacuum

The force transducer is a device that is subjected to the force to be measured and changes it into another measurable physical quantity through a known relationship.There are several groups of force transducers that use different physical relationships. These transducers are based on piezoelectric phenomenon, light pressure [37], magneto-elasticity [38], vibration, surface waves, gyroscopic effect, electromagnetic watt balance [39], etc. Many force transducers employ some form of elastic load-bearing element with known load-deformation behaviour.Elastic devices represent the most common type of a force transducer, while the most frequent method is to make measurements of the longitudinal and lateral strain. When a force is applied to the elastic element it deflects and the deformation is measured by a displacement transducer. Displacement means moving from one position of the object to another for a specific distance or angle referencing to its own prior position rather than to an external reference [36].

Elastic devices are made of materials which exhibit a linear relationship between the stress and strain with low hysteresis and low creep in the working range such as metal alloys (beryllium copper, phosphor bronze, Monel, Inconel, high-carbon and alloyed steel, amorphous metals, etc.), silicon, borosilicate glass, etc. and are perfectly compatible with ultrahigh vacuum conditions. The shape of elastic elements depends on a number of factors including the range of force to be measured, required performance, sensitivity to misalignments and buckling of the displacement transducer coupled to the elastic elements, etc.

Among different geometries of elastic elements of force transducers the most commonly used are the bending beam, cantilever or leaf spring arranged perpendicularly to the direction of acting force to be measured (**Figure 6**) [34,40]. A cantilever employed in Atomic Force Microscopy is an example of a single beam that is used for measuring of forces in two directions. **Figure 7** shows a set-up developed for microtribological measurements and consisting of two parallel beams [41–43].

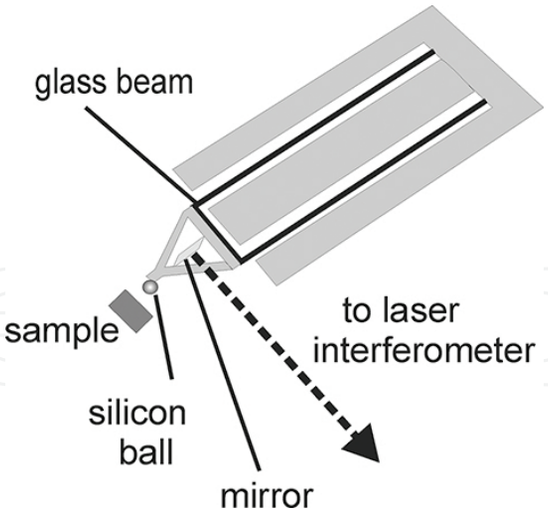

Figure 6. Schematic drawing of a double-leaf spring made of glass and used for simultaneous measurement of normal and tangential forces in a microtribometer. (Reprinted from [42] Copyright 2003, with permission from Elsevier.)

The important disadvantage of a single beam configuration is that under applied load the free end of the beam undergoes both displacement and tilting (**Figure 7**). In some cases tilting is undesirable since it can lead to systematic errors in some displacement transducers.

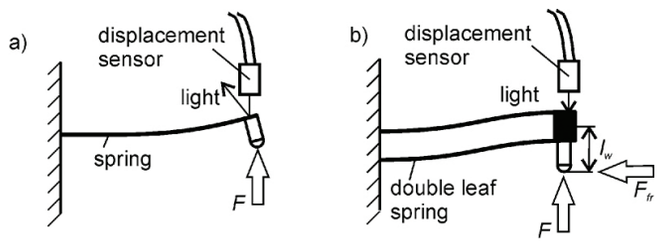

Figure 7. Schematic drawing of a force sensor with a single leaf spring (a) and double-leaf spring (b). (Reprinted from [4] Copyright 2015, with permission from Elsevier.)

Double-leaf spring with two or more parallel beams with their free ends rigidly connected to a block are nearly free of this disadvantage and follows approximately straight displacements [44]. Further improvements of the spring linearity and reducing tilting were achieved by using symmetrical double-leaf configuration with two couples of springs facing each other on both sides of a point, where the force is applied. **Figure 8** shows a complex elastic element designed for measuring of two perpendicular forces [45] using four compliant units (A-D) and their respective mirrored compliant units (A′-D′). The operation of the unit has been described as the following: *When the normal force is applied the Flexure B, B′ and D, D′ would bend to give the desired displacement and Flexure A, A′ and C, C′ are in tensile/compressive load. Similarly, when the lateral force is applied flexure A, A′ and C, C′ deflects to give the desired motion and Flexure B, B′ and D, D′ are in tensile/compressive load. Any parasitic errors due to bending of compound flexures are compensated by the secondary motion stage. Furthermore, this force measuring mechanism is relatively insensitive to thermal disturbances and manufacturing errors due to its symmetry.*

http://dx.doi.org/10.5772/62386

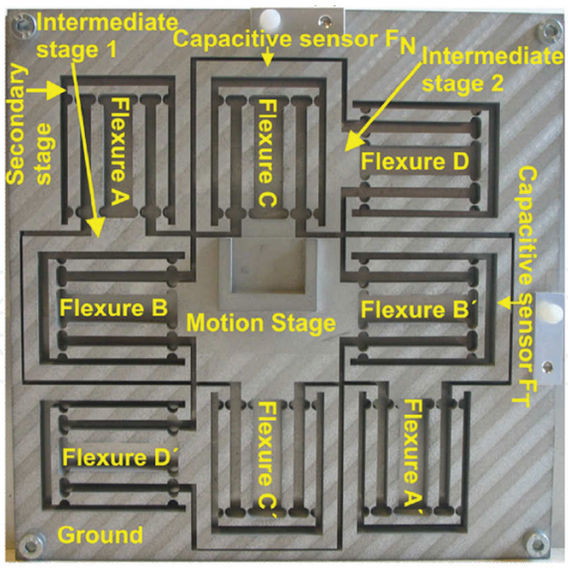

Figure 8. Elastic element for measuring two perpendicular forces using four compliant symmetric double-leaf units. (Reprinted from [45]).

A number of force transducers employing elastic elements in the form of parallel double-leaf spring have been developed and patented so far for atmosphere and vacuum tribometry [41,43,46–50]. A different approach was proposed to measure 3D forces by a single elastic element having a shape of a hollow elastic dome [51]. Deformation of the dome is sensed by a photodiode matrix situated at the circular baseplate of the dome.

Sensing displacement of the elastic element in vacuum can be done by almost any kind of displacement transducer. Strain gauge technology has been the most prominent on the market since its inception in 1938. Other types of displacement transducers include capacitive [34,52, 53], laser interferometry [54], Doppler sensor [55], linear variable differential transformer, optical fibre strain gauge, interference-optical load cell, and so on. An optical displacement transducers is preferable when some sensitive devices are used for physic-chemical characterization. A fibre-optic displacement sensor based on the principle of reflective light intensity modulation is a simple, contactless and compact transducer suitable for operating under vacuum and extreme environments [41,42,56–60]. The basic principles and uncertainty analysis of this type of the sensors are discussed in the following section.

4.2. Intensity modulated bundle fibre-optic displacement sensor

Intensity modulation fibre-optic displacement sensor (IMFODS) consists of one or several transmitting and one or several receiving step-index optic fibres packed in a bundle. At the proximal end the transmitting fibres are illuminated by a light source. Light passed through the transmitting fibres exits their distal end and is reflected from the surface, a distance to which is being measured (**Figure 9**). It is assumed that the reflection is pure specular; thus, the irradiance distribution function at the image plane is the same as for the radiant emittance at the exit from the transmitting fibre. Then the reflected light is coupled to the receiving fibre and directed to a photodiode detector to measure its power. Displacement of the

reflecting surface towards or backwards the distal end of the bundle will modulate the radiant power of light entering the receiving fibres, thus producing variable electrical signal on the photodiode [61,62]. A thorough explanation of the operating principles of the intensity modulation optic fibre displacement sensors is given in the literature [56,62–64].

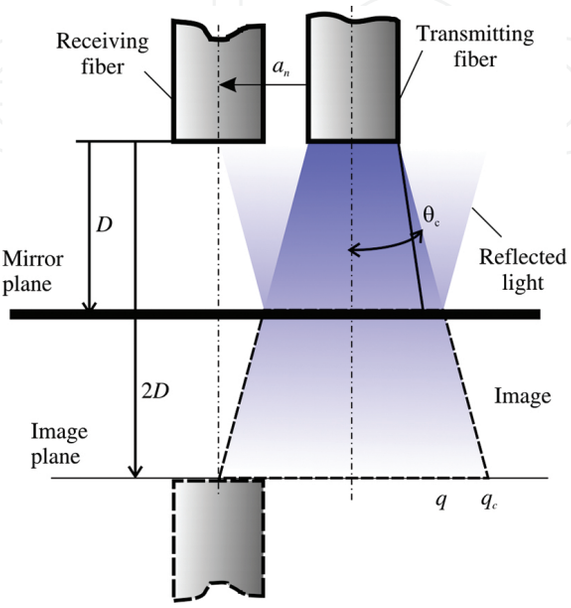

Figure 9. Geometrical considerations of a two-fibre sensor.

The irradiance distribution function at the image plane and the configuration of the receiving and transmitting fibres within a bundle provide the necessary information to determine the sensor modulation characteristic, i.e., the electrical signal at the photodiode detector vs. displacement.

Normally, IMFODSs have two measurement regions: one at near side (front slope) and another at far side (back slope) of the modulation characteristic (**Figure 10**).

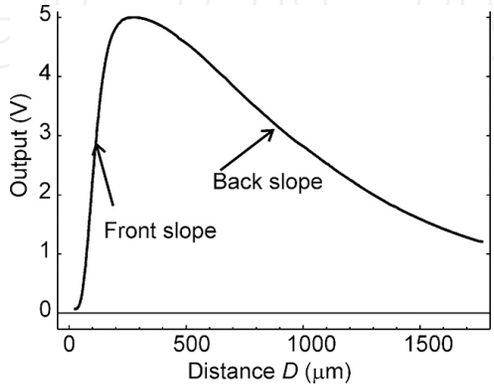

Figure 10. Typical characteristic of IMFODS.

http://dx.doi.org/10.5772/62386

It is gener0ally assumed that both regions are linear. So, when the slope K, of a linear region is known, displacement of the target surface, Δl, can be easily determined from the difference in the output voltage at the final, U_f, and initial, U_i, positions of the target surface [65]:

$$\Delta l = K\left(U_f - U_i\right) \tag{1}$$

Assuming that the measurements of output voltage at the initial and final positions are independent and have the same uncertainty, u_u, the uncertainty in the displacement measurement is found from the following expression [65]:

$$u_{\Delta l} = \Delta l \sqrt{\frac{u_K^2}{K^2} + 2\frac{u_U^2}{\left(U_f - U_i\right)^2}} \tag{2}$$

where u_K is the uncertainty of K.

Although linear assumption is useful for practical applications, the measurement uncertainty is quite large since the characteristics of IMFODS are not perfectly linear in both ranges [65]. In addition, linear regions are quite narrow as compared with the total available measurement range. All these limit the applicability of this approach.

Another approach is based on the displacement determination directly from the modulation characteristic without any assumption on its form [65]:

$$\Delta l = l\left(U_f\right) - l\left(U_i\right) \tag{3}$$

where $l(U_z)$ is the distance between the sensor and the target surface corresponding to the output voltage U_z.

In this approach an inverse modulation characteristic l=$g(U)$ is used. $g(U)$ is a monotonous function with two existence domains corresponding to front and back slopes of normal modulation characteristic.

The corresponding uncertainty is [65]:

$$u_{\Delta l} = \sqrt{u_{l(U_f)}^2 + u_{l(U_i)}^2} \tag{4}$$

where $u_{l(U)}$ is the uncertainty in the determination of distance $l(U)$.

Measurement uncertainty can be found experimentally in each point of the modulation characteristics or from the uncertainty of the normal modulation characteristic, $u_{f(l)}$, using the following transformation [65]:

$$u_{l(U)} = \frac{\sqrt{u_{f(l)}^2 - u_U^2}}{df(l)/dl} \tag{5}$$

In most cases the uncertainty in the voltage reading is much below the uncertainty of the modulation characteristic, so (5) can be simplified:

$$u_{l(U)} \approx \frac{u_{f(l)}}{\left|df(l)/dl\right|} \tag{6}$$

These formulae indicate that knowledge of the modulation characteristic is required for displacement measurement and determination of its uncertainty.

So far, several models were developed for modulation characteristic of a single pair of fibres and different irradiance distribution function: uniform [56,62,66,67], Gaussian [61,64,68], modified Gaussian [69,70], uniangular [63], theoretical [56]. Though these models showed good correlation with the experimental results, most of them have not been studied for multiple bundled fibres. Cao and co-workers [64] developed a model for the optical fibre bundle displacement sensor for several bundle configurations assuming quasi-Gaussian irradiance distribution function. The quasi-Gaussian, i.e., truncated Gaussian, distribution was adopted by these authors assuming that it coincides best with the actual facts, though, no argument for this assumption were presented. He and Cuomo [56] developed a more realistic theoretical irradiance distribution function for the lossless step-index multimode fibre illuminated with a Lambertian light source. This model is based on the assumption that each light ray propagating through the optical fibre core at different angles with respect to the fibre axis carries the same power. The model was validated for a bundle of seven fibres (six receiving fibres surrounding a transmitting one) with core radius 50 μm and the displacement range between 0 and 900 μm.

Before getting deeper into modelling the coordinates and geometrical considerations must be defined. It is assumed that light exits the transmitting fibre with a conical shape with a critical angle θ_c (**Figures 9** and **11**). The radius of a light spot at the image plane is a function of distance D between the distal end of the bundle and the reflecting surface:

$$q_c = x_0 + 2D\tan\theta_c \tag{7}$$

and corresponding dimensionless critical radius:

$$k_c = \frac{q_c}{x_0} = 1 + \frac{2D}{x_0}\tan\theta_c \tag{8}$$

http://dx.doi.org/10.5772/62386

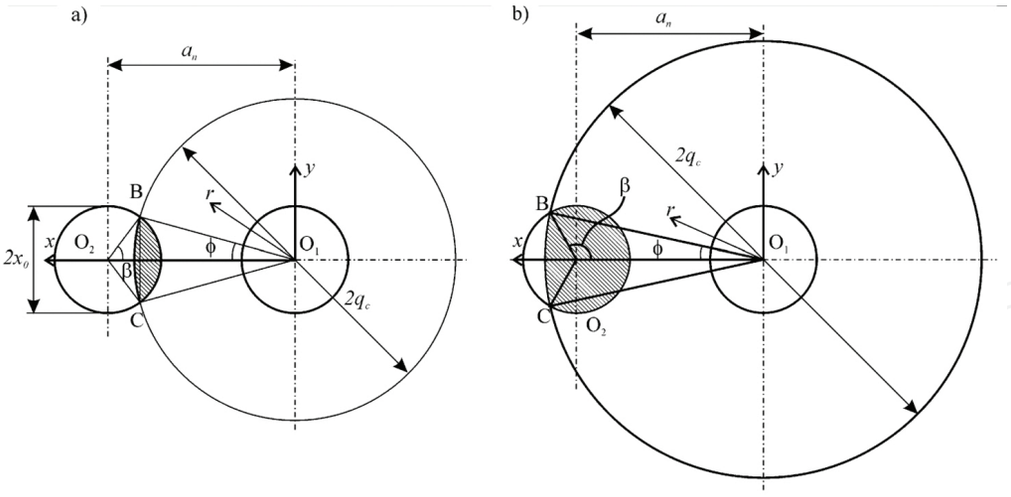

Figure 11. Geometry for determination of subtended area for a pair of fibres placed at a_n distance an between their centres.

The distance between the centres of adjacent fibres depends on the core diameter and the cladding thickness: $a_a = 2(c_l + x_0)$, whereas for any other pair of fibres within a bundle the distance between the fibre centres a_n is a function of the bundle configuration. The corresponding dimensionless distance is $m = a_n/x_0$. For simulation purpose, m was varied proportionally to the dimensionless distance between the centres of the adjacent fibres that in our case was 20/9.

The reflected light collected by a receiving fibre depends on the subtended area, S_i, and the irradiance distribution function, I_i, there on. The subtended area shown by the shadowed region in **Figure 11** is determined as function of only geometrical parameters from the following expression:

$$S_i\left(D,\theta_c\right) = x_0^2\left(k_c^2\varphi + \sin^{-1}\left(k_c\sin\varphi\right) - mk_c\sin\varphi\right),\ k_c \le \sqrt{m^2+1} \tag{9a}$$

$$S_i\left(D,\theta_c\right) = x_0^2\left(k_c^2\varphi + \pi - \sin^{-1}\left(k_c\sin\varphi\right) - mk_c\sin\varphi\right),\sqrt{m^2+1} < k_c < m+1 \tag{9b}$$

where

$$\varphi = \cos^{-1}\left(\left(k_c^2 + m^2 - 1\right)/2k_cm\right). \tag{10}$$

The above model is a further development of more simple models that account only for certain fixed distance between the fibres [63,67,69,70]. In addition, this model corrects some errors present in [63].

The received radiant power is calculated by integration the irradiance distribution function over the subtended area (**Figure 11**):

$$P_{ig} = \int_{S_i} I_i dS = x_0^2 \int_{m-1}^{k_{\max}} I_i k \cos^{-1} \frac{k^2 + m^2 - 1}{2km} dk \tag{11}$$

where $k_{max} = m + 1$ or $k_{max} = k_c$ whichever is smaller.

In the simplest case the irradiance distribution function is assumed uniform over the light spot. Then, assuming the reflection losses negligible, the irradiance at the image plane is determined as follows:

$$I_{iu} = I_0 \frac{x_0^2}{q_c^2} \tag{12}$$

where I_0 is mean radiant emittance at the exit from the transmitting fibre.

The radiant flux directed to the photodiode detector is given by the following expressions in dimensionless form:

$$\frac{P_i}{I_0 x_0^2} = k_c^{-2} \left(k_c^2 \varphi + \sin^{-1} \left(k_c \sin \varphi \right) - m k_c \sin \varphi \right), \; k_c \le \sqrt{m^2 + 1} \tag{13a}$$

$$\frac{P_i}{I_0 x_0^2} = k_c^{-2} \left(k_c^2 \varphi + \pi - \sin^{-1} \left(k_c \sin \varphi \right) - m k_c \sin \varphi \right), \; \sqrt{m^2 + 1} < k_c < m + 1 \tag{13b}$$

$$\frac{P_i}{I_0 x_0^2} = \pi k_c^{-2} k_c > m + 1 \tag{13c}$$

In more complex model the irradiance distribution is simulated by Gaussian function [61]:

$$I_{ig}(k) = \frac{I_0}{k_c^2} \exp\left(-\frac{k^2}{k_c^2} \right) \tag{14}$$

After substitution (14) in (11) the received radiant power can be obtained by integration in polar coordinates:

$$\frac{P_{ig}}{I_0 x_0^2} = 2k_c^{-2} \int_{m-1}^{k_{\max}} \exp\left(-\frac{k^2}{k_c^2}\right) k \cos^{-1} \frac{k^2 + m^2 - 1}{2km} dk \tag{15}$$

Finally, the most realistic theoretical irradiance function was developed by He and Cuomo [56] as a piecewise-defined smooth function composed of eight formulas. These formulas combine according to the values of the parameters k and k_c. Five of these formulas correspond to the interval $k \geq 1$:

$$I_{it}(k) = \frac{I_0 d}{2\theta_c\left(d^2 - 1\right)}\left(\tan^{-1}\left(k_c - 1\right) - \tan^{-1}\left(k - 1\right) + d^{-1}\left(\tan^{-1}\frac{k-1}{d} - \tan^{-1}\frac{k_c - 1}{d}\right)\right), 1 \leq k_c \leq 2 \text{and} 1 \leq k \leq k_c \tag{16a}$$

$$I_{it}(k) = \frac{I_0 d}{2\theta_c\left(d^2 - 1\right)}\left(\frac{\pi}{4} - d^{-1}\tan^{-1} d^{-1} - \tan^{-1}\left(k - 1\right) + d^{-1}\tan^{-1}\frac{k-1}{d}\right) + \frac{I_0}{8\theta_c d}\ln\frac{\left(k_c - 1\right)^2\left(1 + \mathrm{d}^{-2}\right)}{1 + \mathrm{d}^{-2}\left(k_c - 1\right)^2}, k_c > 2, 1 \leq k \leq 2 \text{and} k \geq k_c - 2; \tag{16b}$$

$$I_{it}(k) = \frac{I_0 d}{2\theta_c\left(d^2 - 1\right)}\left(\frac{\pi}{4} - d^{-1}\tan^{-1} d^{-1}\tan^{-1}\left(k - 1\right) + d^{-1}\tan^{-1}\frac{k-1}{d}\right) + \frac{I_0}{8\theta_c d} In\frac{\left(k - 1\right)^2\left(1 + d^{-2}\right)}{1 + d^{-2}\left(k - 1\right)^2}, \mathrm{k}_c > 2, 1 \leq k \leq 2 \text{and} k < k_c - 2; \tag{16c}$$

$$I_{it}(k) = \frac{I_0}{8\theta_c d}\ln\frac{\left(k_c - 1\right)^2\left(1 + d^{-2}\left(k - 1\right)^2\right)}{\left(k - 1\right)^2\left(1 + d^{-2}\left(k_c - 1\right)^2\right)}, k_c > 2, k > 2 \text{and} k \geq k_c - 2; \tag{16d}$$

$$I_{it}(k) = \frac{I_0}{8\theta_c d}\ln\frac{\left(k + 1\right)^2\left(1 + d^{-2}\left(k - 1\right)^2\right)}{\left(k - 1\right)^2\left(1 + d^{-2}\left(k + 1\right)^2\right)}, k_c > 2, k > 2 \text{and} k < k_c - 2; \tag{16e}$$

where $d = 2D/x_0$.

The radiant power received by the receiving fibre was calculated numerically in dimensionless form for three irradiation distribution function. The results are given in **Figure 12**.

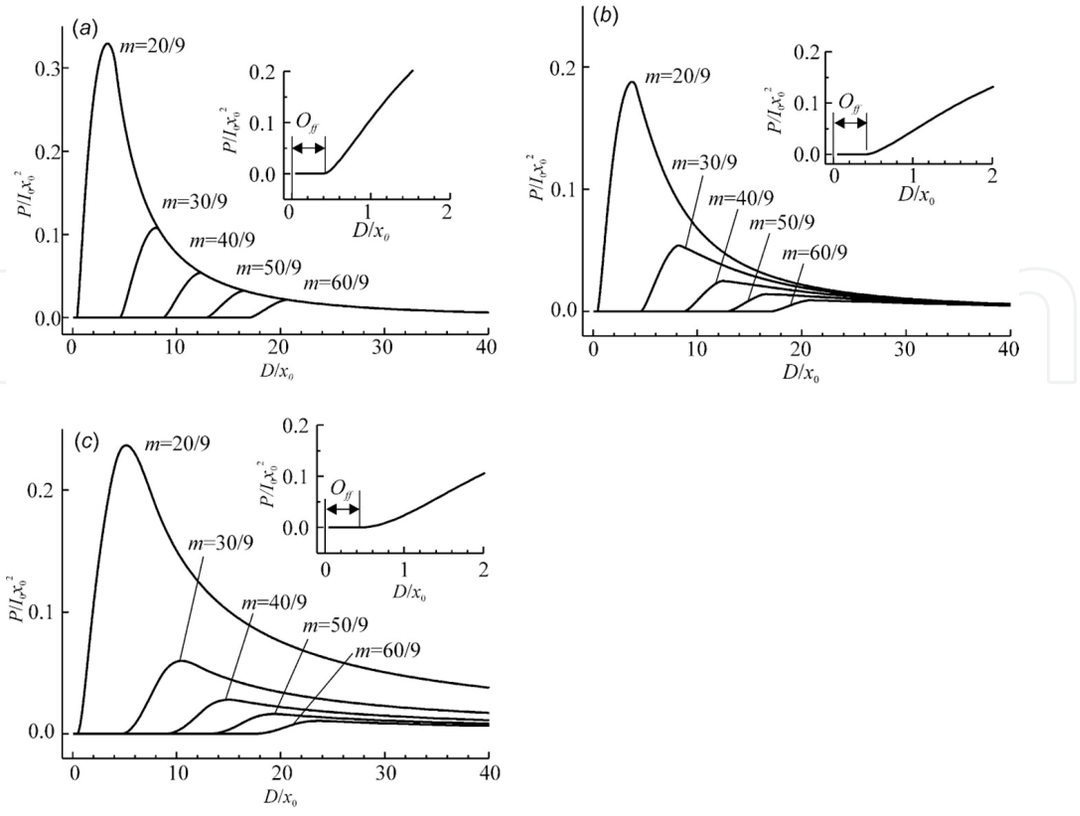

Figure 12. Elemental two-fibre modulation characteristics for various light intensity distribution functions: a) uniform, b) Gaussian, c) He-Cuomo theoretical distribution. Insets show the offset (blind) regions. (Reprinted from [65] Copyright 2013, IOP Publishing.)

The graphs of dimensionless received radiant power vs. D/x_0 for uniform irradiance function show a horizontal offset at the origin, O_{ff}, that increases with increasing m (**Figure 12a**). The offset in dimensionless form can be determined from the following expression:

$$O_{ff} = \frac{m-2}{2\tan\theta_c} \tag{17}$$

For adjacent fibres $O_{ffa} = \frac{c_l}{2\tan\theta_c}$, i.e., is proportional to the cladding thickness. When m increases the value at the maximum decreases and the peak gets less sharp. The falling edges of all peaks converge to the function $(D/x_0)^{-2}$.

For Gaussian irradiance distribution function, the falling edge of all graphs is much more gradual as compared with the uniform irradiance model and all the graphs converge at larger displacements than for the uniform irradiance model (**Figure 12b**).

The graphs for He-Cuomo irradiance model are much less sharp as compared to other models considered above. After reaching the maximum the graphs decrease but do not converge in the studied range of D. For all irradiance distribution functions, the offset of the graphs is the

http://dx.doi.org/10.5772/62386

same since it depends only on the cladding thickness; however, for He-Cuomo model the graph raises very smoothly just after the offset, thus creating illusion of a bigger offset.

To compare the resulting graphs the plots for m=20/9 were normalized dividing by the corresponding maximum values (**Figure 13**). The position of the maximum shifts to larger D/x_0 in the following order: Uniform ,*U*, Gaussian, *G*, He-Cuomo, *H-C*, models. Also, the slopes of the front and falling edges of the peaks decrease following the same order. It should be mentioned that for He-Cuomo model the falling edge of the peak is much higher at larger distances than for other two models.

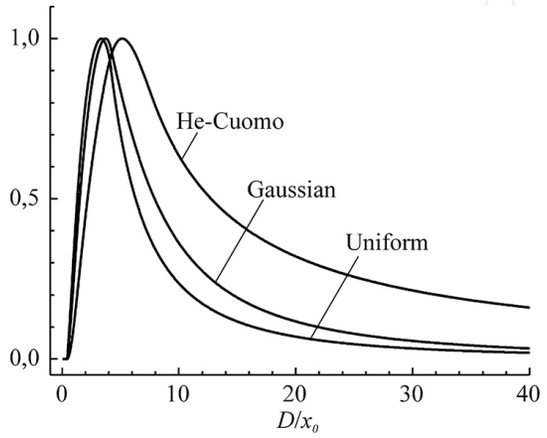

Figure 13. Normalized received radiant power for Uniform, Gaussian and He-Cuomo irradiance functions.

In many cases the transducers have more than one of each transmitting and receiving fibres assembled in a bundle. Independently of the order of the fibres in the bundle, the resulting signal of the photodiode detector can be found as a superposition of the signals from the individual receiving fibres. In turn, the signal on a receiving fibre is proportional to a sum of the received radiant power from each transmitting fibre. Therefore, the total voltage at the photodiode detector can be determined by summation [65]:

$$U(D) = \sum_{l=1}^{l=N_r} U_r(D) \propto \sum_{l=1}^{l=N_r} \sum_{j=1}^{j=N_t} P_i(l,j,D) \tag{18}$$

where $P_i(l,j,D)$ is the radiant power from the j-th transmitting fibre subtended by the l-th receiving fibre at a distance D from the reflecting surface, N_t is the number of transmitting fibres and N_r is the number of receiving fibres.

The output voltage of the sensor depends not only on the distance to the reflecting surface and the irradiance function but also on $a_n(l,j)$, i.e., on the configuration of the fibres within a bundle.

A summation model for equally spaced fibres with 1×2 periodicity was developed in [64]. It is worth mentioning that the adjacent fibres contribute most significantly to the rising front of the resulting modulation characteristics of the sensor.

The effect of bundle configuration was modelled for a bundle containing 85 fibres with a fibre core radius x_0 = 22.5 μm and cladding thickness c_l = 2.5. Geometry and enumeration of individual fibres in the bundle are shown in **Figure 14**.

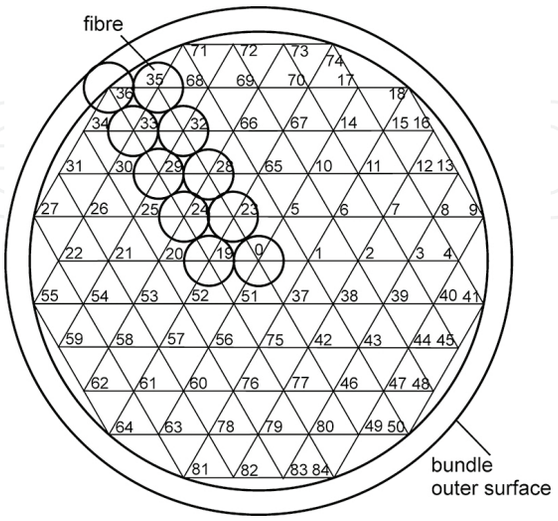

Figure 14. Three bundle configurations were modelled The numbers denote the centres of individual fibres.

The following three configurations of a bundle were modelled: alternating linear configuration of fibres (a line of transmitting fibres followed by a line of receiving fibres and so on), semicircle, and random configuration. The results for alternating linear configuration and for the semicircular one are shown in **Figure 15**.

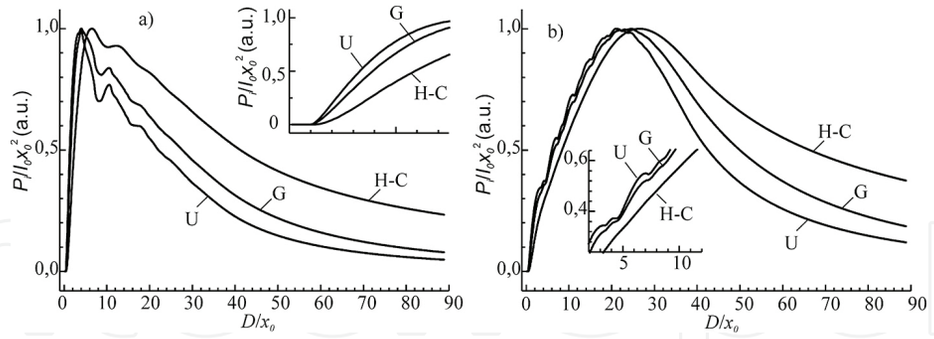

Figure 15. Modulation characteristics of a IMFODS with a) alternating linear configuration of transmitting and receiving fibres; b) semicircle configuration of emitting and receiving fibres. U – uniform irradiance function; G – Gaussian irradiance model; H-C – He-Cuomo theoretical irradiance function.

For the alternating configuration of fibres, there is a large number of transmitting fibres situated at a short distance from the receiving ones. Therefore, for all three irradiance distribution functions the plots have sharp peaks at the falling edge resulting from the contribution of the nearby transmitting fibres. However, for He-Cuomo function these peaks are less important than for other functions. A similar effect can also be observed for the semicircle configuration (**Figure 15b**). Whereas the sensor is being retracted from the reflecting surface

http://dx.doi.org/10.5772/62386

new rows of receiving and transmitting fibres enter synchronously into the light spot at the image plane producing sharp steps on the modulation characteristic. Again, for He-Cuomo model the graphs are smoother than for other irradiance distribution functions.

Earlier Cao et al. [64] simulated modulation characteristics of an IMFODS using various bundle configurations including the "random" one. In fact, the configuration they referred to as "random" was an ordered one with a definite pattern (see **Figure 2** in [64]). In this work, real random distribution of the fibres was obtained using a random number generator. Five different random configurations were created. **Figure 16** a shows mean modulation characteristic determined as a mean of five particular modulation characteristics corresponding to five random bundle configurations. In addition, standard deviation and error of mean were determined for all models. Despite the use of random configuration followed by averaging of particular modulation characteristics, the graphs in **Figure 16** for uniform and Gaussian models have important corrugation in the region near to the maximum. However, He-Cuomo model gives very smooth modulation curve without any significant peaks and corrugation.

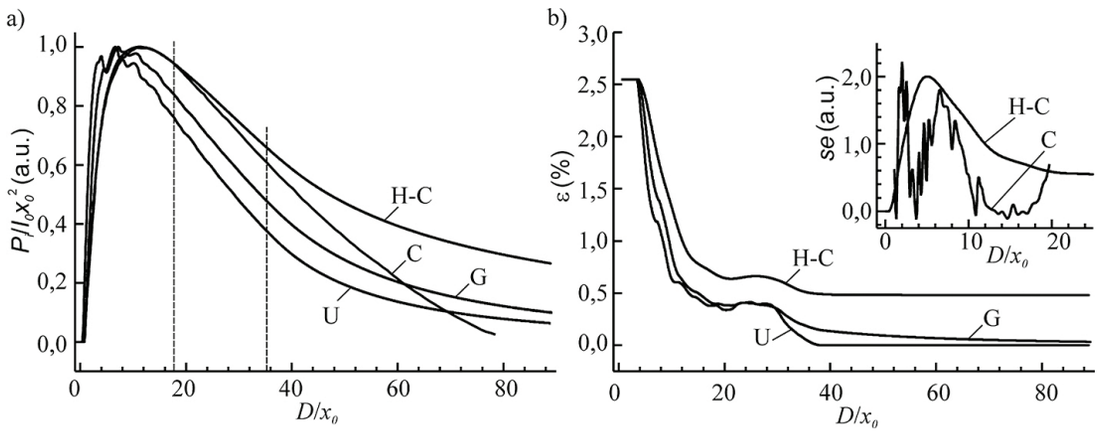

Figure 16. a) Mean modulation characteristic of a bundle optical fibre displacement sensor with random configuration of transmitting and receiving fibres. Portion of graphs fitted by linear function is shown by vertical dashed lines. C – experimental data, U – uniform model, G – Gaussian model, H-C – He-Cuomo theoretical model. b) Relative standard error for random configuration of a bundle and different irradiation distribution functions. Inset: Absolute dimensionless value of standard error for random configuration and He-Cuomo theoretical irradiation distribution. Graph C is the difference between the mean modulation characteristic and the experimental data.

Graph C in **Figure 16** a represents experimental calibration graph of a bundle optical fibre sensor. This graph is well fitted by the He-Cuomo modulation characteristic within the interval of dimensionless displacements from 0 to 20. This finding is consistent with the results published earlier by He and Cuomo [3] in the same range of dimensionless distances. The absolute difference between the two graphs (C) and the standard error for He-Cuomo model (H-C) are plotted in the inset in **Figure 16b**. The standard error reflects dispersion of the mean modulation characteristic related to variation of the bundle configuration. Within the interval of displacements from 3 to 20 the absolute difference between the theoretical and experimental graphs does not exceed standard error, thus indicating that this difference is due to mismatch between the theoretical and real bundle configurations. A sharp peak at the beginning can be

attributed to the experimental error related to limited measurement capacity of the experimental test rig. At the displacements larger than 18 graph C sharply increases indicating significant divergence between two graphs. The slope of the H-C graph decreases, whereas the slope of the experimental graph remains almost constant (**Figure 16a**). Surprisingly, the experimental calibration curve cannot be fitted on the entire range of the displacement using only He-Cuomo theoretical model.

In the range of D/x_0 between 18 and 35 all the plots, both calculated and the experimental, are almost linear. All graphs were fitted in this range by a linear function using a least-squares method and mean slope and the standard error (se) were determined for these linear functions (see **Table 1**). Adjusted coefficient of determination for all fittings was larger than 0.99. The mean slope of the experimental calibration graph is very close to that of the Gaussian model, although the difference between the mean slopes is statistically significant.

Symbol	Uniform	Gaussian	He-Cuomo	Calibration
Mean slope	-2.22×10^{-2}	-2.08×10^{-2}	-1.63×10^{-2}	-1.91×10^{-2}
se	3.64×10^{-5}	2.08×10^{-5}	1.76×10^{-5}	7.36×10^{-5}
Sample volume	426	426	426	32

Table 1. Mean slope of fitted linear functions, standard error of the slope (*se*) and the sample volume for calculated modulation characteristics and experimental calibration graph.

Seemingly, the reason for the discrepancy between the calculated and the experimental modulation characteristics should be sought in some discrepancy between the real irradiance distribution function and the function used in He-Cuomo model. To fit the experimental data, the real irradiance distribution function should conceivably combine the characteristics of both Gaussian and He-Cuomo functions: the real irradiance distribution function should have a sharp peak at the origin as He-Cuomo function, but this central part should decrease with increasing D/x_0 as rapidly as Gaussian function.

It was reported that the experimental graph of the measurement uncertainty vs. distance is almost identical to the simulated one obtained by varying the bundle configuration [65]. Bearing in mind that the bundle configuration was constant during the test it was suggested that small imperfections on the mirror surface could be responsible. In fact, presence of spots that reduce reflectivity can alter particular contributions from certain pairs of receiving and transmitting fibres that is equivalent to changing of the bundle configuration. The imperfections should have the size beyond a certain critical value, which is comparable with the fibre core diameter.

Another important conclusion that has been drawn from this study is that, in contrast to implicit expectations [71], the derivatives of the modulation characteristics have no flat features at the near side that suggests absence of nominally linear region. Thus, using the linear approach at the near side will lead to systematic errors related with the deviation from linearity of the modulation characteristic. The values of these errors depend on the displacement range

http://dx.doi.org/10.5772/62386

as well as on the initial and final positions. However, at the far side the derivatives of both theoretical and experimental modulation characteristics have definite flat region, especially at D/x_0 between 30 and 50. Therefore, the using of the linear approach is justified at this side.

5. Concluding remarks

Technological advances in development of precision surface characterization techniques have been notable in the last 20 years offering a wide range of solutions to the research community. Several improvements were achieved thanks to the better understanding of limitations of devices and to the development of reliable measurement techniques pushing the envelope to extreme working conditions. This led to resolving conflicts between different subsystems by means of a holistic approach involving different physic-chemical phenomena. As for complex tribological characterization and indentation, an indirect measurement of the involved forces through displacement measurements is needed, fibre optical and capacitive sensors were found to be the most suitable. The limitations for the former are mainly related to reflectivity loss, critical dependences of the measurement uncertainty on the minute defects on reflecting surfaces, limited temperature range and the non-linearity of its working characteristic; for the latter, a differential capacitive sensor is preferable leading to the need of an active reference. In addition, use of capacitance sensor can be limited when it is used together with other sensitive techniques due to electromagnetic interferences. However, when these kinds of sensors are implemented in the device, their accuracy is so high that the noise floor is recorded and overlaps the measurements. A proper damping is than needed as well as the right models taking into account the estimated instrument cumulated uncertainty. It should then be highlighted the need of subsystem influencing as less as possible these sensors and materials with stable mechanical characteristics over a wide range of temperatures. It is then easy to understand how only non-contact heating device, such as laser-based, inductive or radiation-based heat sources, can be used to such accurate machines, and how important is to keep the measuring device free from external noises and change of temperature.

The results presented in this chapter show that such recommendation are not utopic although a deep experience is needed in interpreting the machine response and proper calibrations should be carried out. As an example, **Figure 17** shows the force measuring head designed by the authors for an ultrahigh vacuum system for tribological characterization of materials and lubricants [4]. The patented head allows measuring two forces in perpendicular directions with very low crosstalk using two pairs of leaf springs. The displacement of the leaf springs is measured by IMFODS mounted on corresponding micropositioning motorized stages. These stages permit not only fine adjustment of the initial position of the IMFODS that is necessary to reduce the measurement uncertainty but also switching from back to front slopes during the experiment. Since the sensitivity of the IMFODS at the front slope is almost tenfold greater than on the back slope, flexibility in selection the range in vacuum offers the opportunity to significantly increase the measurement range.

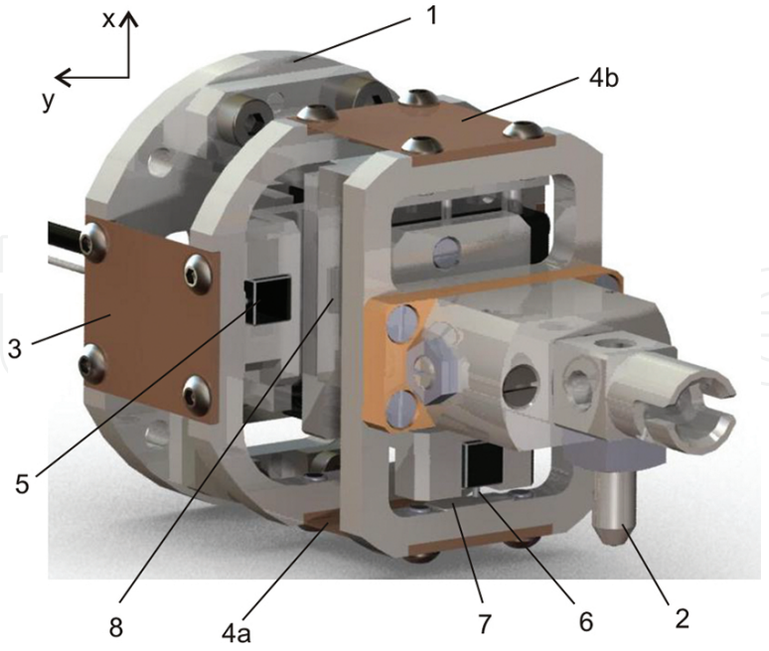

Figure 17. UHV compatible 2-axes force sensor. 1 – the base plate; 2 – the pin; 3 – one of the two leaf-springs used for measuring y component of the force ;4a and 4b – the leaf-springs for measuring x component of the force; 5,6 – IM-FODS; 7 – mirror of the x-stage; and 8 – microactuator for positioning of the optical sensor of the y-stage. (Reprinted from [4] Copyright 2015, with permission from Elsevier.)

Author details

Roman Nevshupa[1*] and Marcello Conte[2*]

*Address all correspondence to: r.nevshupa@csic.es and marcello.conte@anton-paar.com

1 Spanish National Research Council, Institute of Constructional Sciences "Eduardo Torroja" (IETCC-CSIC), Madrid, Spain

2 Anton Paar Tritec SA, Peseux, Switzerland

References

[1] Jones WR, Jansen MJ. Space tribology. Hanover, MD: NASA Center for Aerospace Information; 2000. p. 33.

[2] Miyoshi K. Solid lubricants and coatings for extreme environments: State-of-the-art survey. Technical memorandum. Cleveland, Ohio: National Aeronautics and Space Administration, Glenn Research Center; 2007. p. 16.

[3] Buckley DH. Friction, wear, and lubrication in vacuum. Washington, D.C.: Scientific and Technical Information Office, National Aeronautics and Space Administration; 1971.

[4] Nevshupa RA, Conte M, Igartua A, Roman E, de Segovia JL. Ultrahigh vacuum system for advanced tribology studies: Design principles and applications. Tribology International. 2015;86:28-35. DOI: 10.1016/j.triboint.2015.01.020

[5] ESAE. Space product assurance. Thermal vacuum outgassing test for the screening of space materials. Noordwijk: ECSS Secretariat, ESA-ESTEC; 2008. p. 45.

[6] Fischer D. Untersuchung von reibungsvorschungen mit hlfe der exoelektronenemission. Berlin: Berlin Technical University; 1970.

[7] Vanhulsel A, Velasco F, Jacobs R, Eersels L, Havermans D, Roberts EW, et al. Dlc solid lubricant coatings on ball bearings for space applications. Tribology International. 2007;40:1186-1194. DOI: 10.1016/j.triboint.2006.12.005

[8] Roberts EW. Space tribology: Its role in spacecraft mechanisms. Journal of Physics D: Applied Physics. 2012;45:503001.

[9] Roberts EW, Todd MJ. Space and vacuum tribology. Wear. 1990;136:157-167. DOI: 10.1016/0043-1648(90)90078-O

[10] Martin J-M, Bouchet M-IDB, Matta C, Zhang Q, Goddard WA, Okuda S, et al. Gas-phase lubrication of ta-c by glycerol and hydrogen peroxide. Experimental and computer modeling. The Journal of Physical Chemistry C. 2010;114:5003-5011. DOI: 10.1021/jp909940j

[11] Řepa P. Mechanically induced desorption. Vacuum. 1992;43:367-371. DOI: 10.1016/0042-207X(92)90039-Y

[12] Nevshupa RA, Roman E, de Segovia JL. Origin of hydrogen desorption during friction of stainless steel by alumina in ultrahigh vacuum. Journal of Vacuum Science & Technology A. 2008;26:1218-1223. DOI: 10.1116/1.2968682

[13] Nevshupa RA, Roman E, de Segovia JL. Contamination of vacuum environment due to gas emission stimulated by friction. Tribology International. 2013;59:23-29. DOI: 10.1016/j.triboint.2012.07.009

[14] Nakayama K, Nevshupa RA. Plasma generation in a gap around a sliding contact. Journal of Physics D: Applied Physics. 2002;35:L53-L56.

[15] Nevshupa RA. Effect of gas pressure on the triboluminescence and contact electrification under mutual sliding of insulating materials. Journal of Physics D: Applied Physics. 2013;46:185501.

[16] Nevshupa R, Hiratsuka K. Triboluminescence. In: Gnecco E, Meyer E, editors. Fundamentals of friction and wear on the nanoscale: Springer International Publishing; 2015. p. 57-77.

[17] Williams MW. Triboelectric charging of insulating polymers-some new perspectives. Aip Advances. 2012;2. DOI: 010701 10.1063/1.3687233

[18] Walton AJ. Triboluminescence. Advances in Physics. 1977;26:887-948. DOI: 10.1080/00018737700101483

[19] Nakayama K, Ikeda H. Triboemission characteristics of electrons during wear of amorphous carbon and hydrogenated amorphous carbon films in a dry air atmosphere. Wear. 1996;198:71-76. DOI: 10.1016/0043-1648(96)06934-7

[20] Evdokimov VD. Specific features of exoelectron emission during friction of metals. Soviet Physics Journal. 1968;11:11-13. DOI: 10.1007/BF01890910

[21] Mahrova M, Conte M, Roman E, Nevshupa R. Critical insight into mechanochemical and thermal degradation of imidazolium-based ionic liquids with alkyl and mPEG side chains. Journal of physical chemistry C. 2014;118:22544–22552. DOI: 10.1021/jp504946h

[22] Nevshupa R, Ares JR, Fernández JF, del Campo A, Roman E. Tribochemical decomposition of light ionic hydrides at room temperature. The Journal of Physical Chemistry Letters. 2015;6:2780-2785. DOI: 10.1021/acs.jpclett.5b00998

[23] Rusanov A, Nevshupa R, Fontaine J, Martin J-M, Le Mogne T, Elinson V, et al. Probing the tribochemical degradation of hydrogenated amorphous carbon using mechanically stimulated gas emission spectroscopy. Carbon. 2015;81:788-799. DOI: 10.1016/j.carbon.2014.10.026

[24] Le Mogne T, Martin J-M, Grossiord C. Imaging the chemistry of transfer film in aes/xps analytical UHV tribotester. In: Dowson D, editor. Lubrication at the frontier: The role of the interface and surface layers in the thin film and boundary regime. Amsterdam: Elsevier; 1999. p. 413-422.

[25] Kajdas C. General approach to mechanochemistry and its relation to tribochemistry Tribology in engineering Zagreb: InTech; 2013. p. 209-240.

[26] Schuh CA. Nanoindentation studies of materials. Materials Today. 2006;9:32-40. DOI: 10.1016/S1369-7021(06)71495-X

[27] Bhushan B. Handbook of micro/nano tribology. 2nd ed: Taylor & Francis, 1998. 880 p.

[28] Oliver WC, Pharr GM. Measurement of hardness and elastic modulus by instrumented indentation: Advances in understanding and refinements to methodology. Journal of Materials Research. 2004;19:3-20. DOI: 10.1557/jmr.2004.19.1.3

[29] Dao M, Chollacoop N, Van Vliet KJ, Venkatesh TA, Suresh S. Computational modeling of the forward and reverse problems in instrumented sharp indentation. Acta Materialia. 2001;49:3899-3918. DOI: 10.1016/S1359-6454(01)00295-6

[30] Storåkers B, Larsson P-L. On brinell and boussinesq indentation of creeping solids. Journal of the Mechanics and Physics of Solids. 1994;42:307-332. DOI: 10.1016/0022-5096(94)90012-4

[31] Suresh S, Giannakopoulos AE. A new method for estimating residual stresses by instrumented sharp indentation. Acta Materialia. 1998;46:5755-5767. DOI: 10.1016/S1359-6454(98)00226-2

[32] Trenkle JC, Packard CE, Schuh CA. Hot nanoindentation in inert environments. Review of Scientific Instruments. 2010;81:073901. DOI: 10.1063/1.3436633

[33] Guide to the measurement of force. London: Weight and Force Measuring Panel, The Institute of Measurement and Control, 2013. p.

[34] Woirgard J, Bellaton B, Consiglio R. Measuring head for nanoindentation instrument and measuring method using same. International patent number US7685868 B2. Priority date: 23.12.2004

[35] Nohava J, Randall NX, Conte N. Novel ultra nanoindentation method with extremely low thermal drift: Principles and experimental results. Journal of Materials Research. 2009;24:873-882. DOI: 10.1557/jmr.2009.0114

[36] Fraden J. Position, displacement, and level. Handbook of modern sensors: Springer New York; 2010. p. 279-326.

[37] Smith SB, Cui Y, Bustamante C. Optical-trap force transducer that operates by direct measurement of light momentum. Methods in enzymology: Academic Press; 2003. p. 134-162.

[38] Ştefănescu D. Magnetoelastic force transducers. Handbook of force transducers. Berlin Heidelberg: Springer 2011. p. 165-184.

[39] Richard LS, Edwin RW, David BN, Ruimin L. Towards an electronic kilogram: An improved measurement of the planck constant and electron mass. Metrologia. 2005;42:431.

[40] Stachowiak G, Batchelor AW. Experimental methods in tribology: Elsevier Science, 2004. p.

[41] Liu H, Bhushan B. Adhesion and friction studies of microelectromechanical systems/nanoelectromechanical systems materials using a novel microtriboapparatus. Journal of Vacuum Science & Technology A. 2003;21:1528-1538. DOI: 10.1116/1.1560711

[42] Nevshupa RA, Scherge M, Ahmed SIU. Transitional microfriction behavior of silicon induced by spontaneous water adsorption. Surface Science. 2003;526:209-209. DOI: 10.1016/S0039-6028(02)02067-8

[43] Scherge M, Schaefer JA. Microtribological investigations of stick/slip phenomena using a novel oscillatory friction and adhesion tester. Tribology Letters. 1998;4:37-42. DOI: 10.1023/a:1019182500536

[44] Brouwer DM, Meijaard JP, Jonker JB. Large deflection stiffness analysis of parallel prismatic leaf-spring flexures taking into account shearing, constrained warping and anticlastic curving effects. Precision engineering. 2013;37:505 - 521.

[45] Yaqoob MA, M.B. R, Schipper DJ. Design of a vacuum based test rig for measuring micro adhesion and friction force. In: De Wilde WP, Brebbia CA, Hernández S, editors. High performance structures and materials vi. Southampton: WIT press; 2012. p. 261-274.

[46] Block B. Solid state force transducer and method of making same. Patent number CA1114644 A1. Priority date: 9 Feb 1976

[47] Uchikawa H, Munekata M, Motohashi H. Kinetofrictional force testing apparatus. Patent number US 5212657. Priority date: 16.01.1990

[48] Hegde SG, Praino AP, Root SJ, Sri-Jayantha M. Tunable feedback transducer for transient friction measurement. Patent number US 5115664. Priority date: 25.06.1990

[49] Börner H, Frindt F, Mollenhauer O, Spaltmann D. Ultrahochvakuum-tribometer. Patent number DE10390125B4. International patent number WO2003060487A1. Priority date: 18.01.2002

[50] Dellah A, Wild PM, Moore TN, Shalaby M, Jeswiet J. An embedded friction sensor based on a strain-gauged diaphragm. Journal of Manufacturing Science and Engineering. 2002;124:523-527. DOI: 10.1115/1.1461839

[51] TarÁS, Cserey GG, Veres J. Sensor device. International patent number WO2013072712 A1. Priority date: 17.11.2011

[52] Bonin WA. Multi-dimensional capacitive transducer. Patent number US 5661235. Priority date: 20.12.1995

[53] Bellaton B, Consiglio R, Woirgard J. Measuring head for nanoindentation instrument and measuring method. Patent application WO2014202551 A1. Priority date: 17.06.2013

[54] Kosinskiy M, Ahmed SI-U, Liu Y, Schaefer JA. A compact reciprocating vacuum microtribometer. Tribology International. 2012;56:81-88. DOI: 10.1016/j.triboint.2012.06.019

[55] Holton C, Ahmadian M. Doppler sensor for the derivation of torsional slip, friction and related parameters. Patent number US7705972 B2. Patent number US7705972 B2. Priority date: 20.06.2006

[56] He G, Cuomo FW. A light intensity function suitable for multimode fiber-optic sensors. Journal of Lightwave Technology. 1991;9:545-551. DOI: 10.1109/50.76670

[57] Mollenhauer O, Scherge M, Karguth A. Device for examining friction conditions. Patent number US 6666066. Priority date: 03.04.1998

[58] Spaltmann D, Boerner H, Frindt F, Mollenhauer O. Tribometer. Patent number WO 03060487. International patent number WO 03060487. Priority date: 20.01.2003

[59] Roman E, Nevshupa R, de Segovia JL, Konovalov PI, Menshikov IP. Method and apparatus for analysis of gas content in solids and surface coatings. Patent number WO2007ES70216 20071220. Priority date: 23.02.2007

[60] Nevshupa R, Conte M, Delgado A, Igartua A, Egaña F, Aranzabe A. Dispositivo de medida de fuerzas. Patent number WO 2011080355. Priority date: 29.12.2009

[61] Weik MH. Fiber optics standard dictionary. New York: Springer US, 1989. 366 p. DOI: 10.1007/978-1-4757-1177-6

[62] Cuomo FW. The analysis of a three-fiber lever transducer. Proceedings of SPIE Symposium. 1984;478:28-32. DOI: 10.1117/12.942653

[63] Cook RO, Hamm CW. Fiber optic lever displacement transducer. Appl Opt. 1979;18:3230-3241. DOI: 10.1364/AO.18.003230

[64] Cao H, Chen Y, Zhou Z, Zhang G. Theoretical and experimental study on the optical fiber bundle displacement sensors. Sensors and Actuators A: Physical. 2007;136:580-587. DOI: 10.1016/j.sna.2006.12.010

[65] Nevshupa R, Conte M, Van Rijn C. Measurement uncertainty of a fibre-optic displacement sensor. Measurement Science and Technology. 2013;24:035104. DOI: 10.1088/0957-0233/24/3/035104

[66] Lawson CM, Tekippe VJ. Fiber-optic diaphragm-curvature pressure transducer. Opt Lett. 1983;8:286-288. DOI: 10.1364/OL.8.000286

[67] Faria JB. A theoretical analysis of the bifurcated fiber bundle displacement sensor. IEEE Transactions on Instrumentation and Measurement. 1998;47:742-747. DOI: 10.1109/19.744340

[68] Samian FRP, Pramono YH, Rohedi AY, Rusydi F, Zaidan AH. Theoretical and experimental study of fiber-optic displacement sensor using multimode fiber coupler. Journal of Optoelectronics and Biomedical Materials. 2009;1:303-308.

[69] Libo Y, Jian P, Tao Y, Guochen H. Analysis of the compensation mechanism of a fiber-optic displacement sensor. Sensors and Actuators A: Physical. 1993;36:177-182. DOI: 10.1016/0924-4247(93)80190-r

[70] Lin C-S, Chang R-S. Fiber optic displacement sensors for the measurement of a vibrating object. Precision Engineering. 1994;16:302-306. DOI: 10.1016/0141-6359(94)90008-6

[71] Buchade PB, Shaligram AD. Influence of fiber geometry on the performance of two-fiber displacement sensor. Sensors and Actuators A: Physical. 2007;136:199-204. DOI: 10.1016/j.sna.2006.11.020

IntechOpen